Article

Attosecond inner-shell lasing at ångström wavelengths

https://doi.org/10.1038/s41586-025-09105-9

Received: 28 August 2024

Accepted: 6 May 2025

Published online: 11 June 2025

Check for updates

Thomas M. Linker[1,2]✉, Aliaksei Halavanau[3], Thomas Kroll[4], Andrei Benediktovitch[5], Yu Zhang[1], Yurina Michine[6], Stasis Chuchurka[5], Zain Abhari[2], Daniele Ronchetti[5,7,8], Thomas Fransson[1,9], Clemens Weninger[10,11], Franklin D. Fuller[10], Andy Aquila[10], Roberto Alonso-Mori[10], Sébastien Boutet[10], Marc W. Guetg[3], Agostino Marinelli[1,3], Alberto A. Lutman[3], Makina Yabashi[12,13], Ichiro Inoue[12,14], Taito Osaka[12], Jumpei Yamada[12,15], Yuichi Inubushi[12,13], Gota Yamaguchi[12], Toru Hara[12], Ganguli Babu[16], Devashish Salpekar[16], Farheen N. Sayed[16], Pulickel M. Ajayan[16], Jan Kern[17], Junko Yano[17], Vittal K. Yachandra[17], Matthias F. Kling[1,10,18], Claudio Pellegrini[3], Hitoki Yoneda[6], Nina Rohringer[5,7] & Uwe Bergmann[2]✉

Since the invention of the laser, nonlinear effects such as filamentation[1], Rabi cycling[2,3] and collective emission[4] have been explored in the optical regime, leading to a wide range of scientific and industrial applications[5–8]. X-ray free-electron lasers (XFELs) have extended many optical techniques to X-rays for their advantages of ångström-scale spatial resolution and elemental specificity[9]. An example is XFEL-driven inner-shell $K\alpha_1$ ($2p_{3/2} \rightarrow 1s_{1/2}$) X-ray lasing in elements ranging from neon to copper, which has been used for nonlinear spectroscopy and development of new X-ray laser sources[10–16]. Here we show that strong lasing effects similar to those in the optical regime can occur at 1.5–2.1 Å wavelengths during high-intensity (>10^{19} W cm^{-2}) XFEL-driven $K\alpha_1$ lasing of copper and manganese. Depending on the temporal XFEL pump pulse substructure, the resulting X-ray pulses (about 10^6–10^8 photons) can exhibit strong spatial inhomogeneities and spectral splitting, inhomogeneities and broadening. Three-dimensional Maxwell–Bloch calculations[17] show that the observed spatial inhomogeneities result from X-ray filamentation and that the broad spectral features are driven by sub-femtosecond Rabi cycling. Our simulations indicate that these X-ray pulses can have pulse lengths of less than 100 attoseconds and coherence properties that provide opportunities for quantum X-ray optics applications.

Strong lasing effects such as filamentation and Rabi cycling have allowed us to develop optical techniques for various uses, from fundamental studies of electrons, atoms, molecules and materials to cutting-edge scientific and industrial laser applications[5–8,18–20]. There has been a growing experimental effort to extend optical nonlinear and strong-field techniques to the X-ray regime with intense ultrashort pulses provided by X-ray free-electron lasers (XFELs). This work includes the generation of multiple core holes[21–28], X-ray-optical wave mixing[29] and X-ray second harmonic generation[30]. There has even been recent work to extend XFEL experiments to the attosecond regime through the development of new bunch compression schemes and soliton-like amplification methods, leading to next-generation attosecond X-ray science[31–39]. Despite these successes, investigation of higher-order nonlinear processes such as filamentation and Rabi cycling has been lacking, especially in the hard X-ray regime—that is, at ångström wavelengths. Extending nonlinear techniques to hard X-rays is essential for samples requiring large penetration depth, spatial resolution and high fluorescence yield offered by hard X-ray excitations[40]. In the optical regime, the physical origin of filamentation and its associated spectral broadening originates from third-order sample nonlinearities predominantly arising from the Kerr effect and plasma generation that modify the refractive index[7]. In the case of hard X-rays, the index of refraction is very close to unity, and filamentation is traditionally not expected to occur. Rabi cycling[2]—the periodic modulation of populations in two-level systems within a time-varying field—has been observed in the extreme ultraviolet (XUV) and soft X-ray range but has not been reported at ångström wavelengths[41–43].

[1]Stanford PULSE Institute, SLAC National Accelerator Laboratory, Menlo Park, CA, USA. [2]Department of Physics, University of Wisconsin–Madison, Madison, WI, USA. [3]Accelerator Research Division, SLAC National Accelerator Laboratory, Menlo Park, CA, USA. [4]Stanford Synchrotron Radiation Lightsource, SLAC National Accelerator Laboratory, Menlo Park, CA, USA. [5]Center for Free-Electron Laser Science, Deutsches Elektronen-Synchrotron, Hamburg, Germany. [6]Institute for Laser Science, The University of Electro-Communications, Tokyo, Japan. [7]Department of Physics, Universität Hamburg, Hamburg, Germany. [8]Max Planck School of Photonics, Friedrich-Schiller University of Jena, Jena, Germany. [9]Department of Theoretical Chemistry and Biology, KTH Royal Institute of Technology, Stockholm, Sweden. [10]Linac Coherent Light Source, SLAC National Accelerator Laboratory, Menlo Park, CA, USA. [11]MAX IV Laboratory, Lund University, Lund, Sweden. [12]RIKEN SPring-8 Center, Sayo-cho, Japan. [13]Japan Synchrotron Radiation Research Institute, Sayo-cho, Japan. [14]Institute for Experimental Physics/CFEL, University of Hamburg, Hamburg, Germany. [15]Graduate School of Engineering, Osaka University, Osaka, Japan. [16]Department of Materials Science and Nano Engineering, Rice University, Houston, TX, USA. [17]Molecular Biophysics and Integrated Bioimaging Division, Lawrence Berkeley National Laboratory, Berkeley, CA, USA. [18]Department of Applied Physics, Stanford University, Stanford, CA, USA. ✉e-mail: tlinker@slac.stanford.edu; ubergmann@wisc.edu

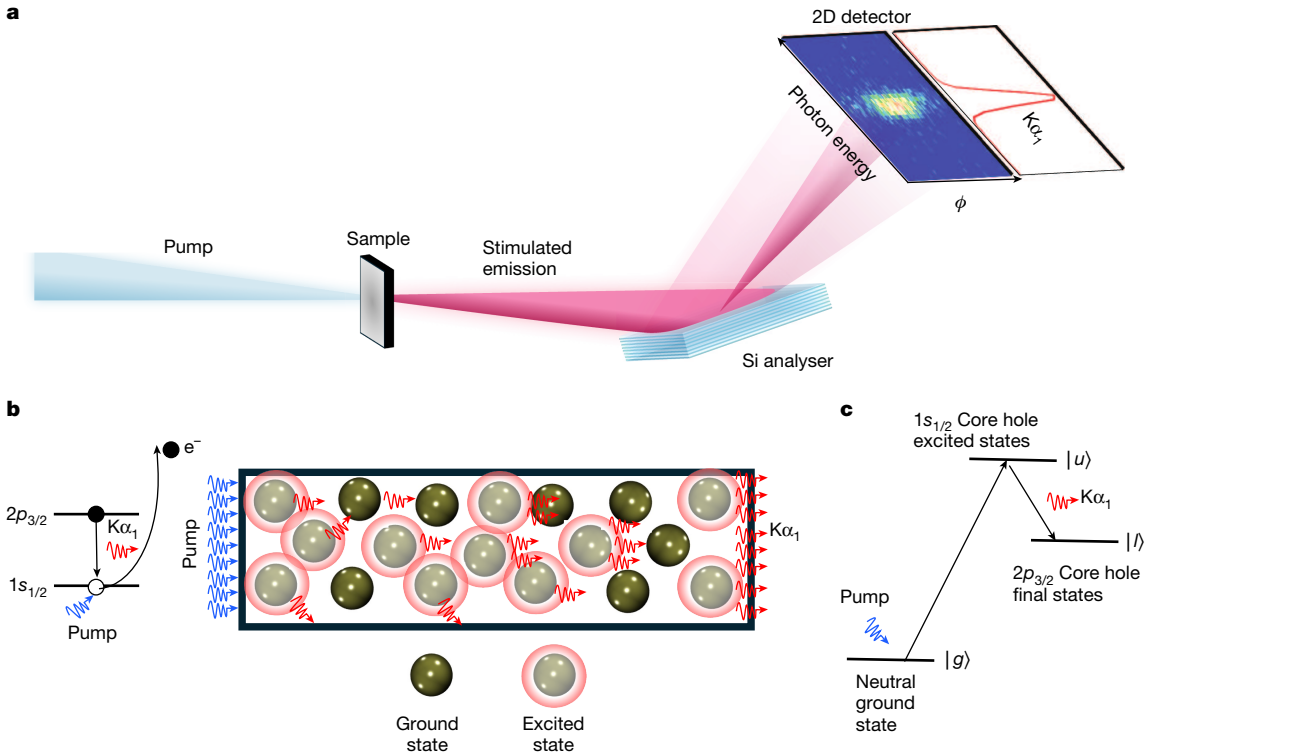

Fig. 1 | Experimental setup and concept of stimulated emission. a, The highly directional stimulated emission signal is analysed with a flat Si(220) crystal with the Bragg angle centred at the Mn or Cu $K\alpha_1$ line followed by a 2D CCD detector. **b**, Stimulated emission process is initiated by a SASE pump pulse ejecting many $1s_{1/2}$ electrons, leading to emission of $K\alpha_1$ photons when $2p_{3/2}$ electrons fill the $1s_{1/2}$ core holes. During stimulated emission, $K\alpha_1$ photons emitted along the forward direction stimulate emission of more $K\alpha_1$ photons, resulting in exponential gain. **c**, State diagram used in the 3D Maxwell–Bloch theory to simulate stimulated emission process. Atoms are excited from an initial ground state $|g\rangle$ to a set of upper levels $|u\rangle$ corresponding to the two possible $1s_{1/2}$ core hole states with differing magnetic quantum ($m = \pm 1/2$). The $K\alpha_1$ transition is to a set of four lower levels $|l\rangle$ corresponding to four possible $2p_{3/2}$ core hole final states with differing magnetic quantum numbers ($m = \pm 3/2, \pm 1/2$).

Here we report the observation and description of laser filamentation and Rabi cycling in superfluorescent inner-shell lasing at the 5.9 keV (2.2 Å) Mn $K\alpha_1$ and 8.05 keV (1.5 Å) Cu $K\alpha_1$ lines. Angular profiles of the stimulated emission analogous to those seen in laser filamentation are observed and determined to be formed from a balance of spontaneous emission, population inversion and self-amplification with diffraction. Direct observation of Rabi frequencies greater than 5 eV is extracted through the self-induced Autler–Townes[44,45] splitting of the stimulated emission spectra, indicating X-ray-induced coherent attosecond population dynamics. Our simulations show that these strong lasing phenomena can lead to the generation of isolated attosecond X-ray pulses, even if the XFEL self-amplified spontaneous emission (SASE) pump pulse is much longer.

Stimulated X-ray emission

The experiments were performed at the nanofocus instrument in Experimental Hutch 5 (EH5) at beamline 3 at the Spring-8 Ångström Compact Free Electron Laser (SACLA) in Hyogo, Japan, and at the Coherent X-ray Imaging instrument at the Linac Coherent Light Source (LCLS) at SLAC National Accelerator Laboratory. Both instruments used highly focused (100–150 nm diameter), intense (on order of 10^{19}–10^{20} W cm^{-2}) SASE XFEL pulses tuned above the K edges of Mn (6.54 keV) and Cu (8.98 keV), respectively. Spectral and angular analysis of the emission signal was performed using a flat Si analyser crystal dispersing the emission signal onto a two-dimensional (2D) charge-coupled device (CCD) detector with one spectral axis and one spatial (angular divergence) axis depending on how the diffraction plane of the Si analyser was aligned to the beam (vertically at LCLS, horizontally at SACLA). The schematics of this geometry, which has been used in previous experiments[12–15], is shown in Fig. 1a. The resulting 2D spectral–angular profiles (2D profiles) in Fig. 1a show the spectral (dispersive) direction indicating the photon energy of the emission signal vertically, and the spatial (non-dispersive) direction, indicating one angular (ϕ) direction of the emission signal for each wavelength relative to the forward direction, horizontally. In this setup, a monochromatic emission signal with large angular divergence (in both directions) would show only a horizontal line in the 2D profile, as the Bragg analyser rejects the angle–wavelength mismatch in the dispersive direction. A broadband emission signal with large angular divergence would give a wide signal in the 2D profile, both vertically and horizontally. As will be seen in the single-shot 2D profiles discussed throughout this paper, strong lasing effects can cause spatial and/or spectral inhomogeneities and broadening. A more detailed description of the experimental setup and parameters is provided in the Supplementary Information.

To model stimulated X-ray emission, we solve the 3D Maxwell–Bloch equations in a continuous variable scheme for the atomic variables as described previously[17]. The stimulated emission process for the $K\alpha_1$ line is shown in Fig. 1b,c, in which an incident SASE XFEL pulse ionizes the Mn/Cu atoms by simultaneously removing many 1*s* electrons, creating an excited state population inversion. A spontaneously emitted $K\alpha_1$ photon resulting from the relaxation of a $2p_{3/2}$ electron into the $1s_{1/2}$ core hole can stimulate the emission of a second $K\alpha_1$ photon along the direction of the core hole excited states. This results in a cascade of amplified spontaneous emission of $K\alpha_1$ photons as shown in Fig. 1b. As the optical path length increases, the influence of the radiation field on the phases of the atomic transition dipoles increases. This causes the transition dipole moments to synchronize, leading to much faster emission, shortening the stimulated emission pulses and enhancing their peak power. As in the optical regime[46], this can eventually lead to Rabi cycling and

generation of pulses much shorter than the excited state (core hole) lifetime. We model the $K\alpha_1$ transition in Mn/Cu with a six-level density matrix consisting of two upper levels $|u\rangle$ corresponding to two possible $1s_{1/2}$ core hole excited states with differing magnetic quantum ($m = \pm 1/2$) and four lower levels $|l\rangle$ corresponding to four possible $2p_{3/2}$ core hole final states with differing magnetic quantum numbers ($m = \pm 3/2, \pm 1/2$). The initial population of the $|u\rangle$ levels is generated by non-resonant photoionization from the initial neutral ground state $|g\rangle$, as shown in Fig. 1c. All relevant ionization, fluorescence and Auger–Meitner decay channels are then considered for the upper and lower levels (see Supplementary Information and ref. 17 for further details).

Filamentation

We first focus on stimulated emission signals primarily exhibiting filamentation qualities without strong spectral broadening. This describes most of the data taken at LCLS, where the peak intensity in the SASE pump pulses was lower than at SACLA. Figure 2a,b shows two examples of 2D profiles for stimulated emission from an $NaMnO_4$ solution measured at LCLS. Although mainly a single spot is seen along ϕ in Fig. 2a, two hotspots are seen in Fig. 2b. In neither case, the dispersive direction shows notable spectral broadening, with most of the signal occurring at the $K\alpha_1$ photon energy. Similar 2D profiles, some with even more than two hotspots, were also observed in $MnCl_2$ solutions and Mn foils at LCLS (Extended Data Fig. 1 and Supplementary Fig. 3). To understand how these hotspots can form during stimulated emission, we first simulate the spectra generated by a single weak SASE spike at solution density. The calculated real-space xy profile of the stimulated emission at the end of propagation through the medium (z-axis is the propagation axis) is plotted in Fig. 2c. The xy profile shows two hotspots along the y-axis, indicative of a filamentation process. To simulate the 2D profiles of our measured signal, we compute the intensity of the far-field stimulated emission and propagate it through the response function of the Bragg analyser (Supplementary Figs. 4 and 5). Figure 2d shows the calculated 2D profile of the stimulated emission, in which the ϕ axis is aligned with the x-axis of the xy profile shown in Fig. 2c. Only one spot is apparent. Figure 2e shows the calculated 2D profile of the stimulated emission, in which the ϕ axis is aligned with the y-axis of the xy profile shown in Fig. 2c, and two spots appear. These calculated 2D profiles shown in Fig. 2d,e are representative of the two measured 2D profiles shown in Fig. 2a,b. This shows that filamentation is detected only in the 2D profile if the hot spots are aligned with the non-dispersive ϕ axis. Filamentation hot spots can occur in any direction, resulting in a variety of inhomogeneities in 2D profiles, but as there is no marked spectral broadening, these inhomogeneities occur mainly along the ϕ axis. As the amplified spontaneous emission process starts from noise, we do not expect simulated 2D profiles to perfectly match any observed 2D profile, but rather to capture the trends.

Figure 2f shows the temporal profile of a simulated Gaussian pump pulse (red) that mimics a single SASE spike (pulse length of about 235 attoseconds full width at half-maximum (FWHM), intensity around 10^{19} W cm^{-2}) and the temporal profile of Mn $K\alpha_1$ stimulated emission (blue) spatially integrated over the transverse axes at the end of the pulse propagation. Our simulation indicates that the stimulated emission pulse generated from the SASE spike under conditions leading to filamentation has approximately 600 attoseconds FWHM pulse length. Snapshots of the filamentation dynamics that lead to the formation of the hotspots are plotted in Fig. 2g, showing several xy profiles of the stimulated emission, as it propagates through the sample. At the beginning of the propagation, the signal is dominated by spontaneous emission, resulting in a wide and random distribution of the emitted radiation in space. As stimulated emission begins to dominate, it focuses towards the centre of the pump power, experiencing a gain guiding effect that creates a high buildup of photons within a bounded region that can be much smaller than the pump focus. In this bounded region, multiple hotspots (filaments) can form as diffraction competes with the field amplification. On exhaustion of the pump, the dynamics become diffraction-dominated, resulting in a nearly free propagation regime (see also Supplementary Video 1).

In both data and simulations, we find the distribution of angular hotspots for a given pump pulse to be highly variable from shot to shot, as these hotspots are determined by quantum fluctuations that seed the spontaneous emission process (see Supplementary Figs. 6–9 for more discussion). In most of the measured shots, we detect only a single amplified mode (Supplementary Fig. 6), but, as shown in Fig. 2d, we are sensitive only to multiple hotspots if they occur along the non-dispersive direction ($y \rightarrow \phi$). Our 3D Maxwell–Bloch simulations, using the full (approximately 30 fs) SASE pump pulses (with multiple spikes) used in the experiments at LCLS, show that the ground state is completely depopulated on the rise of the pump pulse (for more discussion, see Supplementary Fig. 10). This important finding explains why using a single spike to represent the SASE pump pulse in our simulations can well reproduce the 2D profiles measured at LCLS.

Rabi cycling and spectral broadening

We next examine the transition into the stronger lasing regime, in which spectral broadening occurs. We focus our discussion on spectral broadening and self-induced Autler–Townes splitting, noting that we have also observed the formation of Mollow triplets (see Extended Data Fig. 2; for discussion, see the Supplementary Information and Supplementary Figs. 11 and 12). Figure 3a shows the spectral width compared with the number of photons for 29,000 single-shot spectra from $NaMnO_4$ taken at LCLS. A constant spectral width over several orders of magnitude of gain, indicative of the buildup transform-limited pulses[12], is followed by strong spectral broadening beginning at around 10^6 photons per pulse in the saturation regime. Deep in saturation, the main signal is redshifted, exhibiting two peaks, as shown in Fig. 3b. It is important to note that the $K\alpha_2$ emission signal is strongly suppressed in stimulated emission[12] and would appear at 5,887 eV for $NaMnO_4$. The measured 2D profile (Fig. 3b, top) can be simulated using a $NaMnO_4$ solution pumped by a high-intensity single SASE spike displaying the same peak splitting and redshift (Fig. 3b, bottom). The corresponding pulse length is 320 attoseconds FHWM (Supplementary Fig. 17). Shifts or broadening due to the electronic structure of the medium can be ruled out for the origin of the shift and splitting (Supplementary Figs. 13–17 and ref. 12). Furthermore, we see only such pronounced splitting and red shift when entering the strong saturation regime (Supplementary Figs. 13–17). Our simulations show that this spectral feature is a result of the self-induced Autler–Townes splitting, consistent with previous theoretical work[45]. The splitting of about 3.5 eV observed in the spectra measured at LCLS corresponds to the Rabi frequency. At SACLA, where the pump pulse intensity was higher, we observed larger Autler–Townes splittings greater than 5 eV for a 7-μm copper foil and the corresponding simulation yields a 230-attosecond FWHM pulse length (Supplementary Fig. 19). This splitting only occurs when the population is inverted on a time scale much shorter than the core hole lifetime[45], which further indicates that these strong lasing shots are driven by a single strong spike from the SASE pump pulse.

We now show that the observed asymmetry of the Autler–Townes splitting requires both forward and transverse radiation propagating in a highly inverted gain medium. Figure 3c shows the calculated field intensity and phase dynamics for stimulated emission in the high-gain regime (high density and high pump intensity) at the focus of the pump pulse, as well as the fully spatially integrated spectral intensity as a function of the propagation axis. The top row shows the dynamics when transverse propagation of the fields is not included (1D dynamics), and the bottom row shows when it is included (3D dynamics). Both cases exhibit intensity ringing with stronger effects in the 1D case. Similar to the optical regime[46], the ringing is much weaker than the main

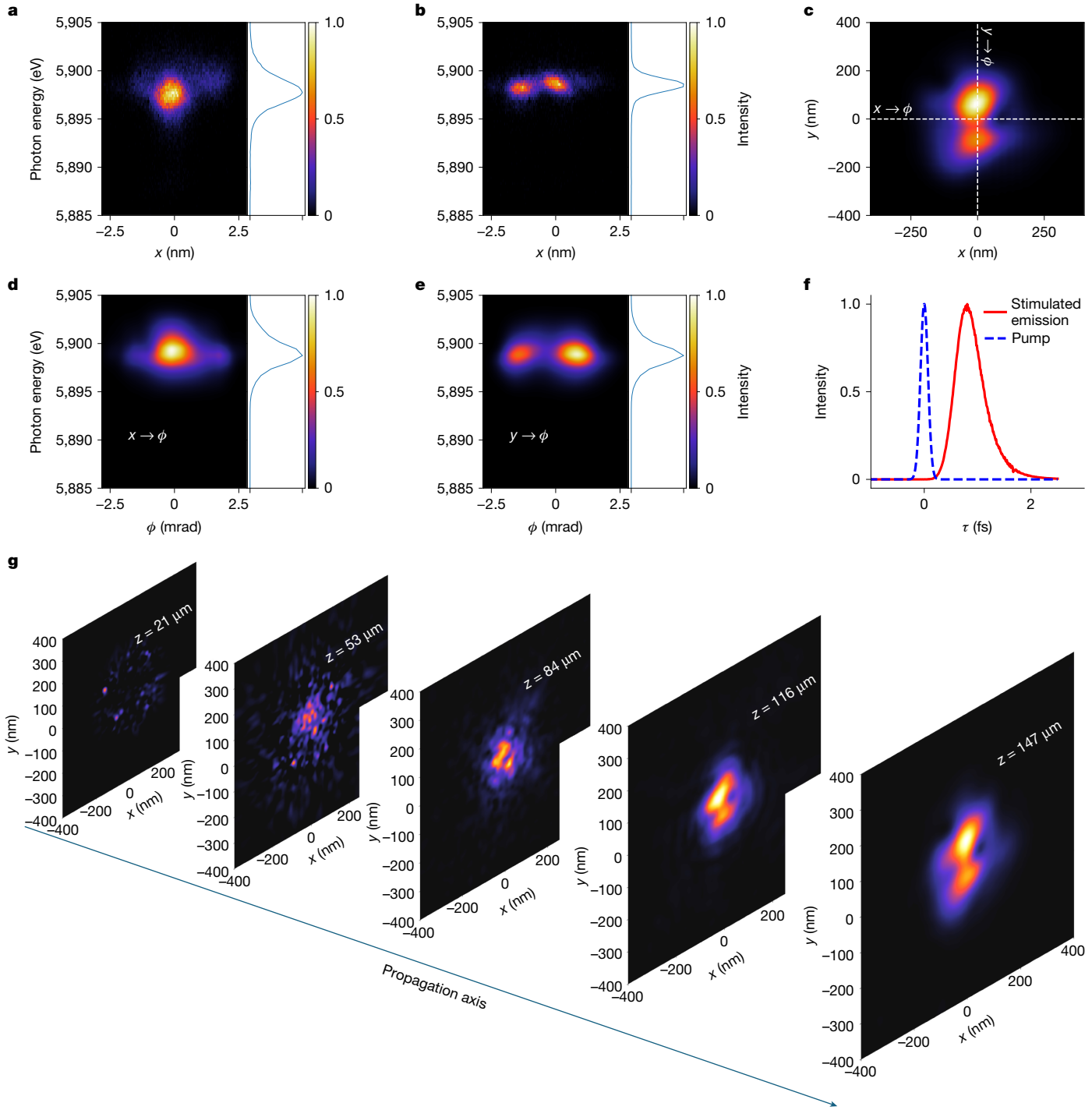

Fig. 2 | Filamentation of stimulated emission. a,**b**, The 2D profiles taken at LCLS for $NaMnO_4$ showing hotspots in their spatial direction (ϕ). **c**, Real-space (xy) simulation of stimulated emission leaving the medium with two hot spots along the y-axis. **d**,**e**, Simulation of 2D profiles based on **c** with the spatial direction (ϕ) corresponding to either the x-axis (**d**) or the y-axis (**e**). The figures show that hot spots are more dominant in the 2D profile when they are aligned with the spatial direction (ϕ). **f**, Temporal profile of pump (dashed) and stimulated emission (red) for simulation shown in **c**. **g**, Snapshots showing xy profile of the stimulated emission simulation shown in **c** as it propagates in the gain medium, showing the self-focusing and filamentation process (see the Supplementary Information for full video).

emission pulse, and the main emission pulse length is much shorter than the excited state (core hole) lifetime. For the 1D dynamics, we see the expected π phase shift in the intensity ringing during Rabi cycling and a corresponding symmetric spectral profile that is not consistent with our measured 2D profiles. For the 3D case, the phase dynamics are much more complex on entering the Rabi cycling regime. This results in intensity ringing with a time-dependent phase, generating a non-symmetric spectral profile, consistent with our measured 2D profiles. We find that the phase is nearly constant within the FWHM of the stimulated emission pulse (Supplementary Fig. 19). Driven deep into saturation, the Autler–Townes splitting becomes washed out, and the spectrum becomes broad and inhomogeneous when 3D dynamics are considered. For these cases, our simulations indicate the pulse lengths are of the order of 100 attoseconds. This is the case for a large fraction of the lasing shots obtained at SACLA, where we found that 78% of all stimulated emission shots from a 20-μm-thick Cu metal foil

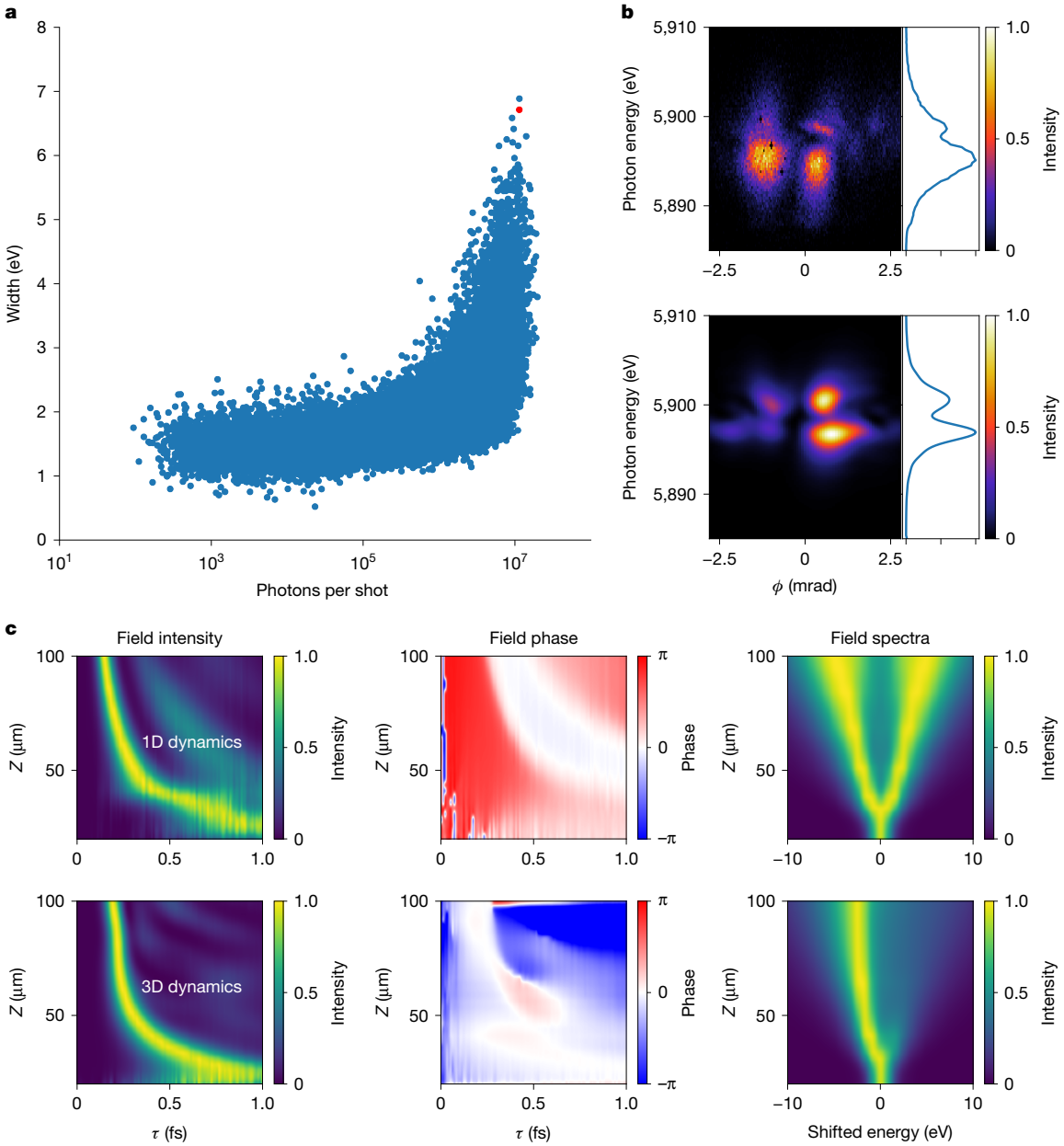

Fig. 3 | Transition to strong lasing and Rabi cycling. a, Measured spectral width compared with the number of stimulated emission photons, indicating transition to strong lasing regime. **b**, Experimental 2D profile for $NaMnO_4$ solution in the strong lasing regime (red point in **a**) with shoulder peak indicative of Autler–Townes splitting (top) compared with simulation showing the same asymmetric splitting (bottom). **c**, Phase dynamics of the stimulated emission. Top, 1D simulation showing symmetric splitting with equal intensity in each emission peak. Bottom, 3D simulation showing modulation during the Rabi cycling resulting in an asymmetric, redshifted spectrum. The Rabi ringing is no longer temporally coherent with the parent emission spike, indicating self-phase modulation of the radiation during 3D propagation. This asymmetry is consistent with the experimental 2D profile (**b**).

displayed broad inhomogeneous spectra (see Extended Data Fig. 3 and discussion in the Supplementary Information).

Figure 4a shows an example of a shot deep in saturation taken at SACLA for a MnO-loaded carbon film. The 2D profile exhibits spatial and spectral inhomogeneities and large spectral broadening. For comparison, a simulation under similar conditions is shown in Fig. 4b. Figure 4c shows the temporal profile of the SASE pump pulse (blue dashed) used for the simulation and the temporal response of the stimulated emission signal (red) resulting in a pulse length of 120 attoseconds FWHM. Here, a single spike of the SASE pump pulse completely depopulates the ground state and drives the emission deep into saturation. The Autler–Townes splitting is washed out, resulting in a broad and inhomogeneous spectrum. We note that the simulation is slightly more spatially inhomogeneous than the experiment. We attribute this to the simulation being performed at the sample average density, whereas the film density was not uniform (Supplementary Information). Figure 4d,g shows further examples of 2D profiles of single shots deep in saturation for an MnO-loaded film and a Cu 20 μm foil. Apart from the spatial and spectral inhomogeneities and large spectral broadening, spectral fringes with regular spacing start to appear in Fig. 4d, and they can be seen more prominently in Fig. 4g. We have previously observed and described 2D profiles exhibiting well-defined spectral fringes for Mn-stimulated emission[15]. These well-defined fringes result from the interference of temporally coherent stimulated emission pulse pairs generated from two separate SASE spikes within the pump pulse. The fringe spacing ΔE is related to the pulse spacing Δt through the Fourier analysis in the Bragg spectrometer with $\Delta t \Delta E = h = 4.136$ fs eV, where h is the Planck's constant. The fringe contrast and envelope depend on the pulse length,

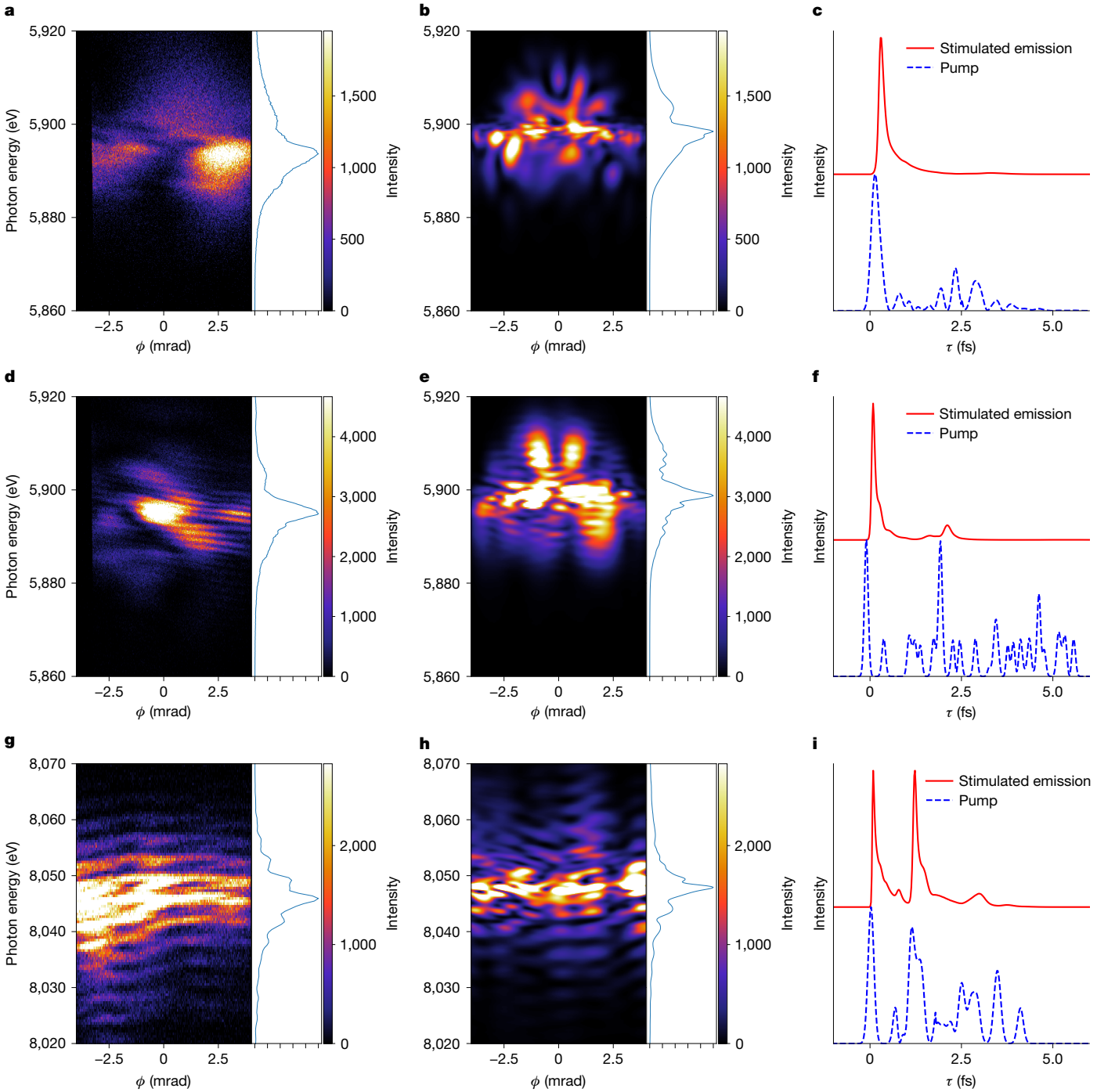

Fig. 4 | Broadening through Rabi cycling at high intensities. a, Experimental 2D profile showing large spatial and spectral inhomogeneities and broadening for MnO film. **b**, Simulation of 2D profile showing similar features using a SASE pump pulse and the same average Mn density as in the experiment (**a**). **c**, Temporal profile of the SASE pump pulse (dashed) and stimulated emission signal (red) used in the simulation showing 120 attosecond FWHM pulse length. **d**, Experimental 2D profile showing large spatial and spectral inhomogeneities and broadening and the onset of spectral fringes with approximately 2 eV spacing for MnO film. **e**, Simulation of 2D profile showing similar features using a SASE pump pulse and the same Mn density as in the experiment (**d**). **f**, Temporal profile of the SASE pump pulse (dashed) and stimulated emission signal (red) used in the simulation (**e**). The resulting signal shows a strong pulse with 100 attosecond FWHM length, and a much smaller second pulse, delayed by about 2 fs, corresponding to the fringe spacing. **g**, Experimental 2D profile showing large spatial and spectral inhomogeneities and broadening and the more pronounced spectral fringes with around 4 eV spacing for Cu foil. **h**, Simulation of 2D profile showing similar features using a SASE pump pulse and the same Cu density as in the experiment (**g**). **i**, Temporal profile of the SASE pump pulse (dashed) and stimulated emission signal (red) used in the simulation (**h**). The resulting signal shows two strong pulses with 90 attoseconds and 100 attoseconds FWHM pulse lengths. The pulses are delayed by about 1 fs, corresponding to approximately 4 eV fringe spacing.

coherence and relative strengths of the two pulses. Figure 4e,h shows simulations of 2D profiles exhibiting fringes comparable to the measured spectra (Fig. 4d,g). Figure 4f,i shows the corresponding temporal profiles of SASE pump pulses (blue dashed) used for the simulations and the temporal profiles of the stimulated emission signals (red). The pulse lengths of the first pulses in the simulated emission signals are 100 attoseconds and 90 attoseconds FWHM, respectively, as shown in Fig. 4f,i. Figure 4f shows that the second emission pulse is 20 times

weaker than the first one, and yet weak fringe contrast can still be seen in the corresponding 2D profile in Fig. 4e. When the second emission pulse has similar intensity and pulse length to the first pulse (Fig. 4i), the corresponding 2D profile is broad and shows fringes with deep contrast (Fig. 4h). In this case, the stimulated emission temporal profile has high intensity displaying pulses with 100 attoseconds FWHM length.

We also observed spectrally broad 2D profiles showing deep fringes with spacings up to 8 eV, corresponding to pulse separations of about 500 attoseconds (Supplementary Fig. 21). As shown in Fig. 4i, multiple deep fringes are indicative of two stimulated emission pulses with similar intensity and length. This is consistent with these pulses having a nearly constant phase (Supplementary Fig. 19). In this case, multiple deep interference fringes can occur only if the length of each pulse in the pair is much shorter than the corresponding temporal spacing, that is, much shorter than 500 attoseconds for an 8-eV fringe spacing.

Conclusions

We have demonstrated how stimulated emission of hard X-rays can be attuned to an optical laser in the strong lasing regime. Our simulations based on 3D Maxwell–Bloch theory[17] show that spatial filamentation is driven through gain guiding effects in the transition from spontaneous to stimulated emission. Spectral broadening is driven by the self-compression of the stimulated emission pulse from Rabi cycling with sub-fs periods. This pulse compression is a key feature of the collective emission during superfluorescence, in which shortening of pulses is accompanied by an increase in their peak power[46]. Rabi cycling is the fundamental building block of most studies of coherent control of quantum systems. In many observed 2D profiles, the extracted Rabi frequencies are greater than 5 eV (<0.86 fs), indicating our ability to drive coherent attosecond inner-shell population dynamics. Controlling these dynamics will be essential for new source development and the next-generation X-ray spectroscopy and quantum optics applications. The recent development of single-spike SASE XFEL pulses[37,39] can help to better control these dynamics and heavier gain mediums with shorter lifetimes (for example, Lα emission of W or Hf at about 8 keV) can potentially generate even shorter pulses well below 100 attoseconds. We are currently working on schemes to spatially and/or spectrally separate the stimulated emission from the pump pulse. As the angular divergence of the stimulated emission pulses is determined by the medium density and overall gain length of the sample, its divergence can be several mrad, which is larger than the divergence of a strongly focused pump pulse. This makes it possible to separate the signal spatially from the pump pulse by choosing an interaction point further downstream. Spectral separation can be achieved using a downstream filter with an absorption edge between the photon energies of the pump pulse and the stimulated emission. For a Cu gain medium, a 50-µm thick Cu foil transmits about 10% of the 8 keV $K\alpha_1$ stimulated emission pulse while transmitting only about 3×10^{-6} of the 9 keV pump pulse.

Online content

Any methods, additional references, Nature Portfolio reporting summaries, source data, extended data, supplementary information, acknowledgements, peer review information; details of author contributions and competing interests; and statements of data and code availability are available at https://doi.org/10.1038/s41586-025-09105-9.

1. Hercher, M. Laser-induced damage in transparent media. *J. Opt. Soc. Am.* **54**, 563 (1964).
2. Rabi, I. I. Space quantization in a gyrating magnetic field. *Phys. Rev.* **51**, 652–654 (1937).
3. Gray, H. R., Whitley, R. M. & Stroud, C. R. J. Coherent trapping of atomic populations. *Opt. Lett.* **3**, 218–220 (1978).
4. Bonifacio, R. & Lugiato, L. Cooperative radiation processes in two-level systems: superfluorescence. *Phys. Rev. A* **11**, 1507–1521 (1975).
5. Boyd, R. W., Gaeta, A. L. & Giese, E. in *Springer Handbook of Atomic, Molecular, and Optical Physics* (ed. Drake, G.) 1097–1110 (Springer, 2008).
6. Couairon, A. & Mysyrowicz, A. Femtosecond filamentation in transparent media. *Phys. Rep.* **441**, 47–189 (2007).
7. Chin, S. L. *Femtosecond Laser Filamentation*, Vol. 55 (Springer, 2010).
8. Ready, J. F. *Industrial Applications of Lasers* (Elsevier, 1997).
9. Chergui, M., Beye, M., Mukamel, S., Svetina, C. & Masciovecchio, C. Progress and prospects in nonlinear extreme-ultraviolet and X-ray optics and spectroscopy. *Nat. Rev. Phys.* **5**, 578–596 (2023).
10. Rohringer, N. et al. Atomic inner-shell X-ray laser at 1.46 nanometres pumped by an X-ray free-electron laser. *Nature* **481**, 488–491 (2012).
11. Yoneda, H. et al. Atomic inner-shell laser at 1.5-ångström wavelength pumped by an X-ray free-electron laser. *Nature* **524**, 446–449 (2015).
12. Kroll, T. et al. Stimulated X-ray emission spectroscopy in transition metal complexes. *Phys. Rev. Lett.* **120**, 133203 (2018).
13. Kroll, T. et al. Observation of seeded Mn Kβ stimulated X-ray emission using two-color X-ray free-electron laser pulses. *Phys. Rev. Lett.* **125**, 037404 (2020).
14. Doyle, M. D. et al. Seeded stimulated X-ray emission at 5.9 keV. *Optica* **10**, 513–519 (2023).
15. Zhang, Y. et al. Generation of intense phase-stable femtosecond hard X-ray pulse pairs. *Proc. Natl Acad. Sci. USA* **119**, e2119616119 (2022).
16. Halavanau, A. et al. Population inversion X-ray laser oscillator. *Proc. Natl Acad. Sci. USA* **117**, 15511–15516 (2020).
17. Chuchurka, S., Benediktovitch, A., Krušič, Š., Halavanau, A. & Rohringer, N. Stochastic modeling of x-ray superfluorescence. *Phys. Rev. A* **109**, 033725 (2024).
18. Qi, P. et al. Sensing with femtosecond laser filamentation. *Sensors* **22**, 7076 (2022).
19. Lee, Y., Oh, S.-W. & Han, S.-H. Laser-induced breakdown spectroscopy (LIBS) of heavy metal ions at the sub-parts per million level in water. *Appl. Spectrosc.* **66**, 1385–1396 (2012).
20. Chin, S. L. et al. Advances in intense femtosecond laser filamentation in air. *Laser Phys.* **22**, 1–53 (2012).
21. Young, L. et al. Femtosecond electronic response of atoms to ultra-intense X-rays. *Nature* **466**, 56–61 (2010).
22. Hoener, M. et al. Ultraintense X-ray induced ionization, dissociation, and frustrated absorption in molecular nitrogen. *Phys. Rev. Lett.* **104**, 253002 (2010).
23. Cryan, J. P. et al. Auger electron angular distribution of double core-hole states in the molecular reference frame. *Phys. Rev. Lett.* **105**, 083004 (2010).
24. Fang, L. et al. Double core-hole production in N_2: beating the Auger clock. *Phys. Rev. Lett.* **105**, 083005 (2010).
25. Berrah, N. et al. Double-core-hole spectroscopy for chemical analysis with an intense X-ray femtosecond laser. *Proc. Natl Acad. Sci. USA* **108**, 16912–16915 (2011).
26. Kanter, E. P. et al. Unveiling and driving hidden resonances with high-fluence, high-intensity X-ray pulses. *Phys. Rev. Lett.* **107**, 233001 (2011).
27. Doumy, G. et al. Nonlinear atomic response to intense ultrashort X rays. *Phys. Rev. Lett.* **106**, 083002 (2011).
28. Rudek, B. et al. Ultra-efficient ionization of heavy atoms by intense X-ray free-electron laser pulses. *Nat. Photon.* **6**, 858–865 (2012).
29. Glover, T. E. et al. X-ray and optical wave mixing. *Nature* **488**, 603–608 (2012).
30. Shwartz, S. et al. X-ray second harmonic generation. *Phys. Rev. Lett.* **112**, 163901 (2014).
31. Huang, S., Ding, Y., Huang, Z. & Qiang, J. Generation of stable subfemtosecond hard x-ray pulses with optimized nonlinear bunch compression. *Phys. Rev. Accel. Beams* **17**, 120703 (2014).
32. Ding Y. Generation of femtosecond to sub-femtosecond x-ray pulses in free-electron lasers. In *Proc. SPIE 9512, Advances in X-ray Free-Electron Lasers Instrumentation III*, Vol. 95121B (SPIE, 2015).
33. Li, S. et al. Characterizing isolated attosecond pulses with angular streaking. *Opt. Express* **26**, 4531–4547 (2018).
34. Duris, J. et al. Tunable isolated attosecond X-ray pulses with gigawatt peak power from a free-electron laser. *Nat. Photon.* **14**, 30–36 (2020).
35. Li, S. et al. Attosecond coherent electron motion in Auger-Meitner decay. *Science* **375**, 285–290 (2022).
36. Guo, Z. et al. Experimental demonstration of attosecond pump–probe spectroscopy with an X-ray free-electron laser. *Nat. Photon.* **18**, 691–697 (2024).
37. Franz, P. et al. Terawatt-scale attosecond X-ray pulses from a cascaded superradiant free-electron laser. *Nat. Photon.* **18**, 698–703 (2024).
38. Driver, T. et al. Attosecond delays in X-ray molecular ionization. *Nature* **632**, 762–767 (2024).
39. Yan, J. et al. Terawatt-attosecond hard X-ray free-electron laser at high repetition rate. *Nat. Photon.* **18**, 1293–1298 (2024).
40. Bergmann, U. Stimulated X-ray emission spectroscopy. *Photosynth. Res.* **162**, 371–384 (2024).
41. Mercadier, L. et al. Evidence of extreme ultraviolet superfluorescence in xenon. *Phys. Rev. Lett.* **123**, 023201 (2019).
42. Benediktovitch, A. et al. Amplified spontaneous emission in the extreme ultraviolet by expanding xenon clusters. *Phys. Rev. A* **101**, 063412 (2020).
43. Nandi, S. et al. Observation of Rabi dynamics with a short-wavelength free-electron laser. *Nature* **608**, 488–493 (2022).
44. Autler, S. H. & Townes, C. H. Stark effect in rapidly varying fields. *Phys. Rev.* **100**, 703–722 (1955).
45. Krušič, Š., Mihelič, A., Bučar, K. & Žitnik, M. Self-induced splitting of x-ray emission lines. *Phys. Rev. A* **102**, 013102 (2020).
46. Gross, M. & Haroche, S. Superradiance: an essay on the theory of collective spontaneous emission. *Phys. Rep.* **93**, 301–396 (1982).

Data availability

The processed experimental data used for generating Figs. 2, 3 and 4 are available at Zenodo (https://doi.org/10.5281/zenodo.15078615)[47].

47. Linker, T. et al. Data for attosecond inner shell lasing at angstrom wavelenghts. *Zenodo* https://doi.org/10.5281/zenodo.15078615 (2025).

Acknowledgements We acknowledge the support from the LCLS and SACLA accelerator groups and their technical and engineering staff. We thank M. Seaberg and M. Hayes from the Coherent X-ray Imaging instrument. The use of Linac Coherent Light Source (LCLS), SLAC National Accelerator Laboratory, is supported by the US Department of Energy (DOE), Office of Science, Basic Energy Sciences (BES) DE-AC02-76SF00515 (T.M.L., Y.Z., T.F., C.W., F.D.F., A.A., R.A.-M., S.B., M.F.K. and U.B.). This work is supported by the US Department of Energy (DOE), Office of Science, Basic Energy Sciences (BES) DE-SC-0023585 (A.H., U.B. and C.P.); Office of Basic Energy Sciences (OBES), Division of Chemical Sciences, Geosciences and Biosciences (CSGB) under contract nos. DE-SC0023270 (T.M.L., Z.A. and U.B.); DE-AC02-05CH11231 (J. Yano and V.K.Y.); DE-SC-0063 (M.F.K.); the National Institutes of Health (NIH) grant nos. GM149528 (V.K.Y.), GM110501 (J. Yano), GM126289 (J.K.) and the Ruth L. Kirschstein National Research Service Award (F32GM116423; F.D.F.). The experiment at SACLA was performed with the approval of the Japan Synchrotron Radiation Research Institute (proposal nos. 2017B8066 and 2024A8055). We acknowledge JPSJ KAKENHI for grant nos. 19K20604, 22KK0233, 23K25131, 24K21199 (II) and 22K1813 (T.O.). I.I. acknowledges the financial support from JST PRESTO (JPMJPR24J1). SSRL Structural Molecular Biology Program is supported by the DOE Office of Biological and Environmental Research and the National Institutes of Health, National Institute of General Medical Sciences (including P41GM103393) (T.K.). The contents of this publication are solely the responsibility of the authors and do not necessarily represent the official views of NIGMS or NIH (T.K.). Computer resources for simulations were provided by the National Energy Research Scientific Computing Center (NERSC), a US DOE Office of Science User Facility located at Lawrence Berkeley National Laboratory, operated under contract no. DEAC02-05CH11231 using NERSC award ERCAP0020725. A.B., S.C. and N.R. acknowledge support from DESY, a member of the Helmholtz Association HGF. S.C. acknowledges the financial support of grant no. HIDSS-0002 DASHH (Data Science in Hamburg–Helmholtz Graduate School for the Structure of Matter). D.R. is part of the Max Planck School of Photonics, supported by the German Federal Ministry of Education and Research (BMBF), the Max Planck Society and the Fraunhofer Society. This work is supported by the Cluster of Excellence 'CUI: Advanced Imaging of Matter' of the Deutsche Forschungsgemeinschaft (DFG)—EXC 2056—project no. 390715994.

Author contributions N.R. and U.B. conceived the original research; J.K., J. Yano, V.K.Y., M.F.K. and C.P. participated in the design of the work. T.M.L., T.K., Y.Z., Y.M., Z.A., D.R., M.Y., I.I., T.O., J. Yamada, Y.I., G.Y., T.H., V.K.Y., H.Y. and U.B. performed the experiments at the SACLA; T.K., T.F., C.W., F.D.F., A.A., R.A.-M., S.B., M.W.G., A.M., A.A.L., V.K.Y. and U.B. performed the experiments at LCLS; G.B., D.S., F.N.S. and P.M.A. provided the Mn-loaded polymer composites for experiments at SACLA; Y.M. and H.Y. provided the Cu sulfate pentahydrate and Cu acetate samples for the experiments at SACLA; T.M.L. performed and analysed the 3D Maxwell–Bloch simulations supported by discussions with A.H., A.B. and S.C.; T.M.L. analysed the experimental data supported by discussions with A.H., A.B. and U.B.; T.M.L. and U.B. wrote the first draft of the paper; all authors participated in discussions and editing of the paper.

Competing interests The authors declare no competing interests.

Additional information

Supplementary information The online version contains supplementary material available at https://doi.org/10.1038/s41586-025-09105-9.

Correspondence and requests for materials should be addressed to Thomas M. Linker or Uwe Bergmann.

Peer review information *Nature* thanks the anonymous reviewers for their contribution to the peer review of this work. Peer reviewer reports are available.

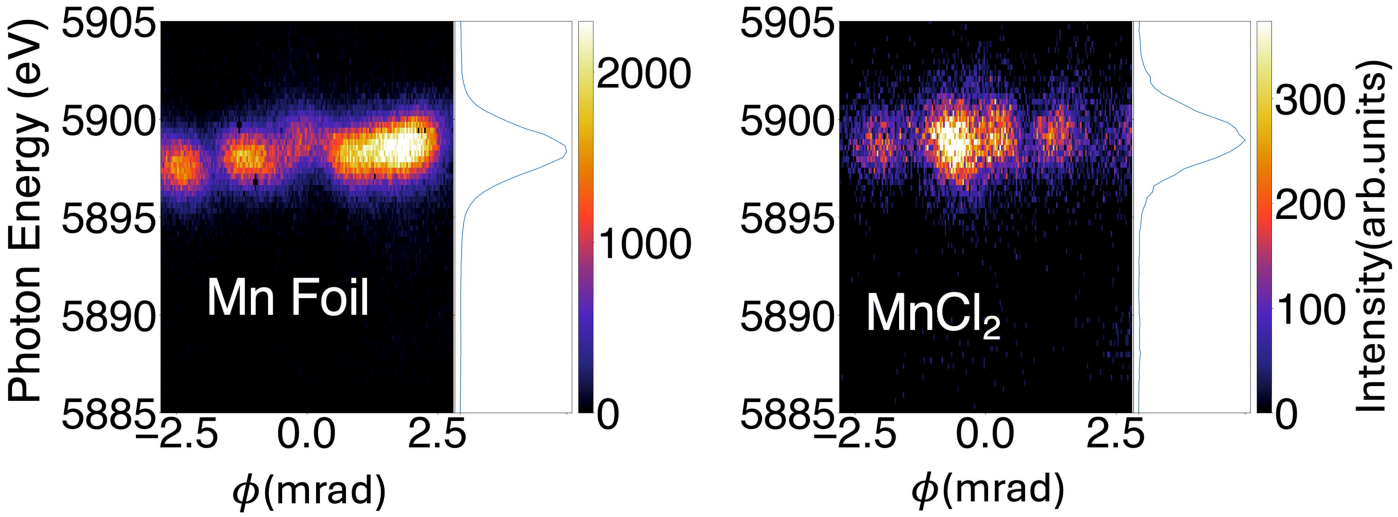

Extended Data Fig. 1 | Filamentation in different samples. Examples of filamentation taken at LCLS for different $MnCl_2$ and Mn metal foils.

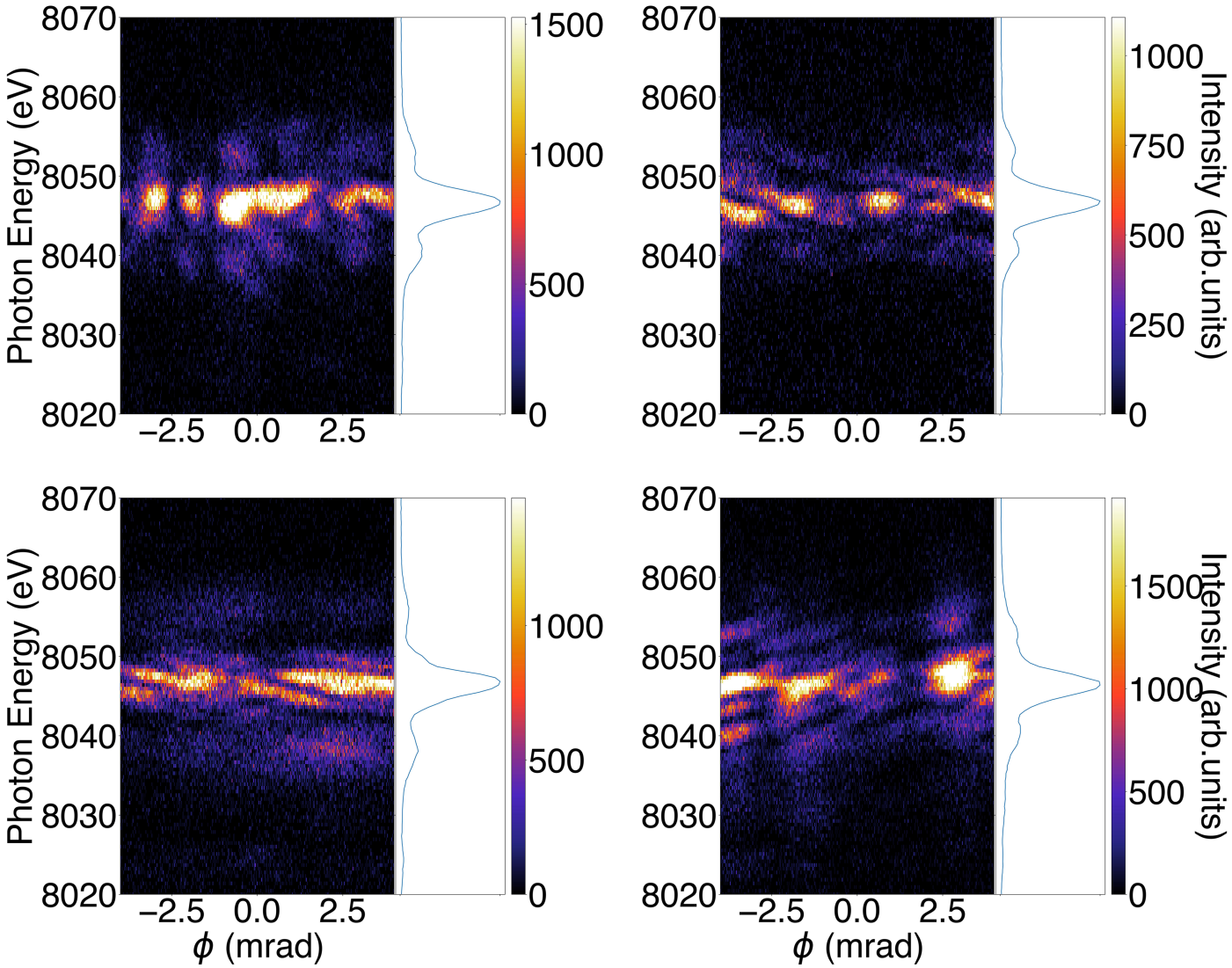

Extended Data Fig. 2 | Observation of Mollow triplets. Examples of Mollow triplets spectra at SACLA taken for Cu 7μm Foils. Further discussion and simulations in the Supplementary Information is provided to describe their formation.

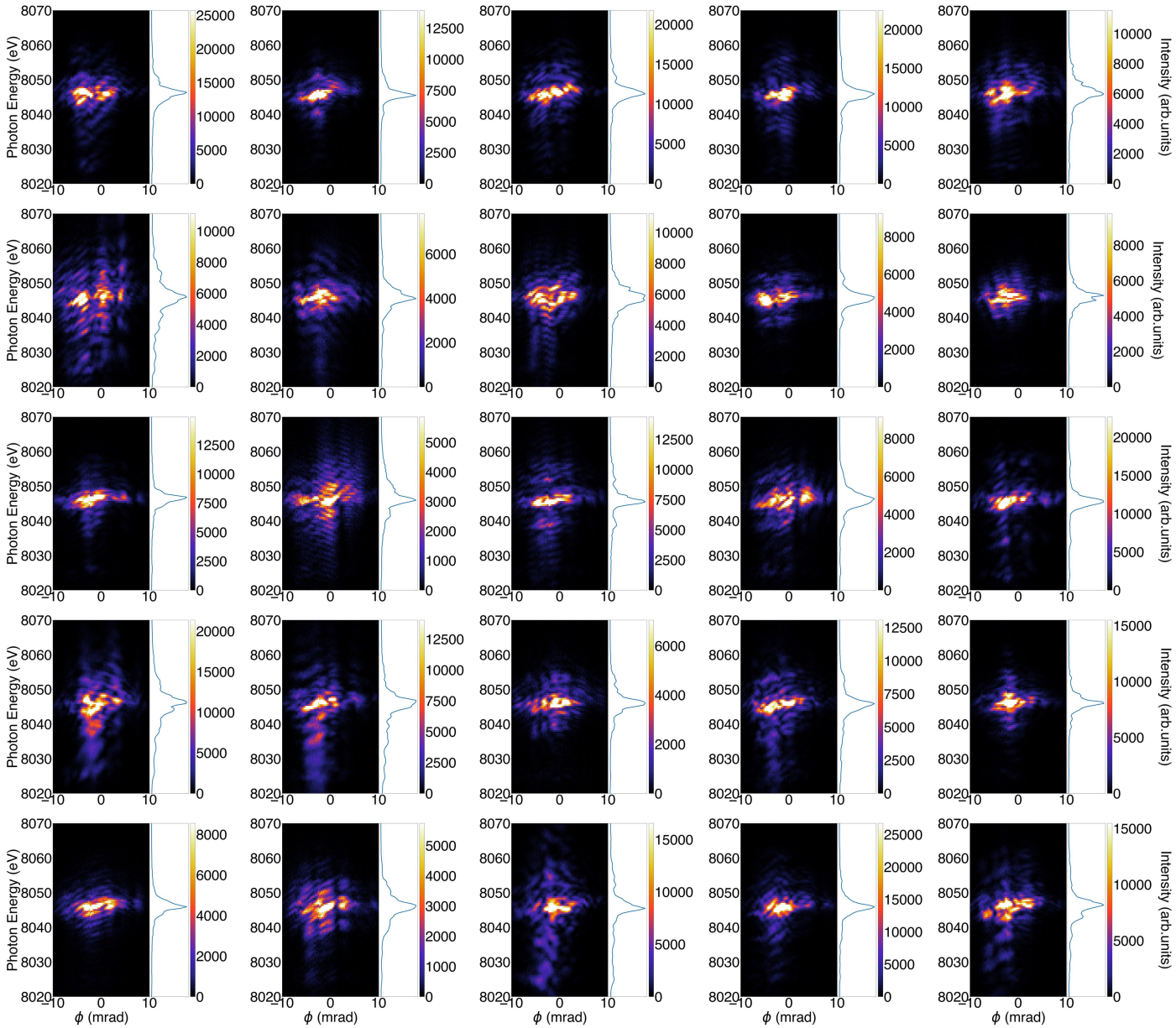

Extended Data Fig. 3 | Typical strong lasing spectra at SACLA. 25 random Strong Lasing Shots for Cu 20 μm Foils which all show broad and inhomogeneous spectra.